2017

Experimental and Multiscale Numerical Studies of Woven Fabric Carbon Composite Cylinder Subjected to Internal Pressure Loading

Kwon, Young W.; Ponshock, Timothy D.; Molitoris, John D.

Springer

Kwon, Young W., Timothy D. Ponshock, and John D. Molitoris. "Experimental and Multiscale Numerical Studies of Woven Fabric Carbon Composite Cylinder Subjected to Internal Pressure Loading." The Structural Integrity of Carbon Fiber Composites. Springer, Cham, 2017. 849-869.

http://hdl.handle.net/10945/66178

Chapter 28
Experimental and Multiscale Numerical Studies of Woven Fabric Carbon Composite Cylinder Subjected to Internal Pressure Loading

Young W. Kwon, Timothy D. Ponshock, and John D. Molitoris

28.1 Introduction

Composite materials have been used increasingly for various applications from sporting equipment to engineering components. Initially, fiber composites were mostly used for applications where stiffness played an important role. As more research continued with better understanding of the material behavior, their applications have been expanded for structural components for which strength is critical. Especially, carbon fiber composites were the major player for the strength applications because of their high strength property. There are too many examples to be mentioned. Examples of large-scale composite structures are commercial and military aircraft and ships. More recently, more extreme loading applications have been studied [1–5] where composite cylinders were used to contain explosive materials.

As composite materials are designed and analyzed for strength application, reliable damage and failure criteria should be used. First of all, failure criteria for fibrous composite materials were developed by modifying those for metallic materials. Because metallic materials are assumed to be isotropic with equal strength in every direction, the failure criteria for metallic materials are based on stress invariants, especially of deviatoric stress components. However, fibrous composite materials have strength which depends on the orientation of the loading relative to the fiber direction. Because fibers are the major load-carrying materials, the strength in the fiber direction is much greater than that in the perpendicular direction.

Y.W. Kwon (✉) • T.D. Ponshock
Naval Postgraduate School, Monterey, CA 93943, USA
e-mail: ywkwon@nps.edu

J.D. Molitoris
Lawrence Livermore National Laboratory, Livermore, CA 94551, USA

P.W.R. Beaumont et al. (eds.), *The Structural Integrity of Carbon Fiber Composites*,
DOI 10.1007/978-3-319-46120-5_28

Additionally, the tensile strength in the fiber direction is generally greater than the compressive strength in the same direction.

Many failure criteria were proposed for fibrous composite materials [6–10]. All those criteria are at the macroscale of the fibrous composite. One failure criterion proposed in Ref. [11] was a second-order polynomial theory for anisotropic materials, and that is expressed as

$$F_i\sigma_i + F_{ij}\sigma_i\sigma_j = 1 \quad i,j = 1,2,\ldots,6 \tag{28.1}$$

where F_i and F_{ij} are the strength parameters to be determined experimentally and σ_i is the stress in the vector format. For an orthotropic lamina under the plane stress condition, Eq. (28.1) is rewritten as

$$F_1\sigma_1 + F_2\sigma_2 + F_6\sigma_6 + F_{11}\sigma_1^2 + F_{22}\sigma_2^2 + F_{66}\sigma_6^2 + 2F_{12}\sigma_1\sigma_2 = 1 \tag{28.2}$$

in which the strength parameters can be determined from the tensile and compressive strength of the fibrous composite in both the fiber direction called X_t and X_c and the transverse orientation called Y_t and Y_c, respectively. In addition, a biaxial test is also required with the stresses $\sigma_1 = \sigma$ and $\sigma_2 = \sigma$. Then, the strength parameters are expressed as

$$F_1 = \frac{1}{X_t} + \frac{1}{X_c} \tag{28.3a}$$

$$F_2 = \frac{1}{Y_t} + \frac{1}{Y_c} \tag{28.3b}$$

$$F_{11} = -\frac{1}{X_tX_c} \tag{28.3c}$$

$$F_{22} = -\frac{1}{Y_tY_c} \tag{28.3d}$$

$$F_{12} = \frac{1}{S_{12}^2} \tag{28.3e}$$

$$F_{12} = \frac{1}{2\sigma^2}\left[1 - \left[\frac{1}{X_t} + \frac{1}{X_c} + \frac{1}{Y_t} + \frac{1}{Y_c}\right]\sigma + \left[\frac{1}{X_tX_c} + \frac{1}{Y_tY_c}\right]\sigma^2\right] \tag{28.3f}$$

where S_{12} is the in-plane shear strength. Later, a revision for the F_{12} was proposed [11] such that

$$F_{12} = -\frac{(F_{11}F_{22})^2}{2} \tag{28.4}$$

Such a failure criterion is a phenomenological expression and does not distinguish different failure modes explicitly such as fiber failure, matrix cracking, and fiber/matrix interface debonding. Another type of failure criterion attempted to distinguish different failure modes. For example, Ref. [6] proposed the following criteria:

$$\left(\frac{\sigma_{11}}{X_t}\right)^2 + \frac{1}{S_c^2}\left({\sigma_{12}}^2 + {\sigma_{13}}^2\right) = 1 \quad \text{for tensile fiber failure} \tag{28.5a}$$

$$\sigma_{11} = X_c \quad \text{for compressive fiber failure} \tag{28.5b}$$

$$\frac{1}{Y_t^2}(\sigma_{22}+\sigma_{33})^2+\frac{1}{S_t^2}\left({\sigma_{23}}^2-\sigma_{22}\sigma_{33}\right)+\frac{1}{S_c^2}\left({\sigma_{12}}^2-{\sigma_{13}}^2\right)=1 \quad \text{for tensile matrix failure} \tag{28.5c}$$

if $(\sigma_{22} + \sigma_{33}) > 0$, and

$$\left[\left(\frac{Y_c}{2S_c}\right)^2 - 1\right](\sigma_{22} + \sigma_{33}) + \frac{1}{4S_t^2}(\sigma_{22} + \sigma_{33})^2 + \frac{1}{S_t^2}\left({\sigma_{23}}^2 - \sigma_{22}\sigma_{33}\right) + \frac{1}{S_c^2}\left({\sigma_{13}}^2 + {\sigma_{13}}^2\right) = 1 \quad \text{for compressive matrix failure} \tag{28.5d}$$

where σ_{13} and σ_{23} are the out-of-plane shear stresses of the lamina, σ_{33} is the normal stress in the thickness direction, and S_t is the transverse shear strength.

The previously mentioned failure criteria are based on the stress components. Alternatively, strain-based failure criteria were also proposed [12]. The stress-based and strain-based criteria can be converted from one to the other, and the equivalence can be shown between them. All those failure criteria required experimental tests at the laminar level. Even though the same fiber and matrix materials were used, the experimental tests would be conducted again if there were a change in the fiber volume fraction. In addition, thermal stresses cannot be properly represented in the failure criteria. For example, let us consider a unidirectional fibrous composite sample without any constraint. The fibrous composite sample has a constant temperature initially. Then, the composite sample is subjected to a uniform heat flux such that the composite reaches another uniform temperature. Because there is no constraint, the composite sample will expand or contract freely depending on the temperature change, and there is no stress at the macroscale level, i.e., at the composite lamina level. However, there are significant stresses at the microscale level because of the mismatch in the coefficients of thermal expansion of the fiber and matrix materials. The stress in one material is in tension, while that in the other material is in compression of the same magnitude such that they cancel each other at the macroscale level. Therefore, such stresses at the constituent material level influence failure loads of the composite sample.

In order to overcome such limitations, new failure criteria were proposed based on multiscale models. In the new criteria, stresses and strains at the constituent

material level are computed, and the failure criteria are applied to those stresses or strains. As a result, more physics-based failure criteria can be expressed with simplified failure modes. The failure criteria based on the constituent material level are described in the next section.

One of composite applications is a pressure vessel or a pipe which can hold internal pressure loading. There has been extensive research for composite pipes under different loading conditions [13–20]. The eventual goal of the present study is to design carbon fiber composite cylinders to contain high explosive materials. In order to achieve the goal, it is necessary to be able to test carbon composite cylinders under internal pressure loading as well as to model and simulate the behavior accurately. Because explosive testing is expensive and risky, it is desirable to minimize live fire testing. Therefore, static internal pressure tests were conducted, and the multiscale modeling was also undertaken to validate the model as the starting point.

In this study, a simple mechanical device was designed and fabricated so that internal pressure loading could be applied using a uniaxial loading frame without using any fluid. The loading device was validated using the finite element analysis (FEA) of the device as well as experiments using aluminum alloy cylinders. Then, the device was used to test carbon fiber composite cylinders for their burst pressure.

Furthermore, the multiscale analysis technique developed in Ref. [21–25] was used to predict the burst strain of the same composite cylinders. The multiscale model begins with the constituent materials such as fibers and the matrix material. Failure criteria were also applied at the constituent materials such as fiber failure in compression or tension, matrix cracking, and fiber/matrix debonding. A composite cylinder subjected to internal pressure experiences tensile loading along the hoop direction. Therefore, the fiber tensile strength was used for the present study.

The next section describes how composite cylinders were fabricated using plain weave composite fabrics. Then, the multiscale analysis model is presented followed by the detailed description of the new mechanical device for internal pressure loading. Subsequently, experimental and numerical studies were conducted for both composite cylinders and tensile test coupons. Finally, conclusions are provided.

28.2 Fabrication of Composite Cylinders

Composite cylinders are usually fabricated using the filament winding technique. Another simple technique is to wrap a woven fabric composite sheet over a cylindrical object. The latter technique was used in this study. Some detailed description of the fabrication process is described below.

The mold was made of a hollow aluminum tube with the outer diameter 7.62 cm (3 in). Two standard metal shelf supports were mounted to a sheet of wood to create a support base for the cylinder form. A large wood dowel was then inserted into the aluminum tube, and screws were used to connect the cylinder form to the support base. A layer of release ply paper and a layer of Teflon sheet were wrapped around

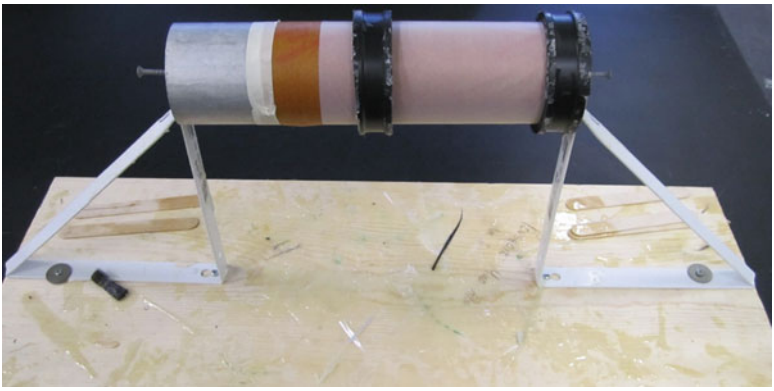

Fig. 28.1 Cylinder mold prepared for composite cylinder layup

the aluminum cylinder in order to ensure an easy release after the fabrication. Then, two rubber couplers were inserted into the aluminum tube so that composite layers would be placed between the two couplers. Figure 28.1 shows the mold prepared for the composite cylinder.

Before wrapping the composite fabric, the resin and hardener were thoroughly mixed in a ratio 4.17 by weight. Following the mixture, the epoxy was applied to either side of the composite fabric for the portion to be used for the first layer as well as the mold rig. This initial application ensures complete epoxy coverage for the first wrap of the fiber strip to minimize voids during the curing process. Next, the composite fabric was wrapped around the cylindrical mold. Before every layer of wrapping, epoxy was applied evenly. Maintaining tension on the fiber strip during the wrapping process is a key to fabricating a uniformly thick cylinder with minimal voids.

Then, a strip of the perforated release ply and the breather cloth were applied to the wrapped composites. The breather cloth absorbs any excess epoxy that is pressed through the perforated release ply. The entire mold cylinder was then removed from the base, and a spiral-wound line was connected between the mold cylinder and a vacuum pump**.** Then, the mold cylinder was inserted into a vacuum bag to take out air from the wrapped composite.

The partially cured composite cylinder was inspected. In order to ensure a uniform thickness and the smooth outer surface, a roller was used and a cylindrical rubber was wrapped tightly around the composite cylinder. The perforated release ply and breather cloth were again used along with a vacuum bag for final curing.

Following the final cure, the composite cylinder and the mold were removed from the vacuum bag, breather cloth, and perforated peel ply. Following removal from the mold, the top and bottom guide and the outer surface form were removed from the composite cylinder, which resulted in the rough cylinder in its both edges as shown in Fig. 28.2. The rough edges were trimmed using a rotary cutting tool to make the final composite cylinders with length of 7.62 cm (3 in).

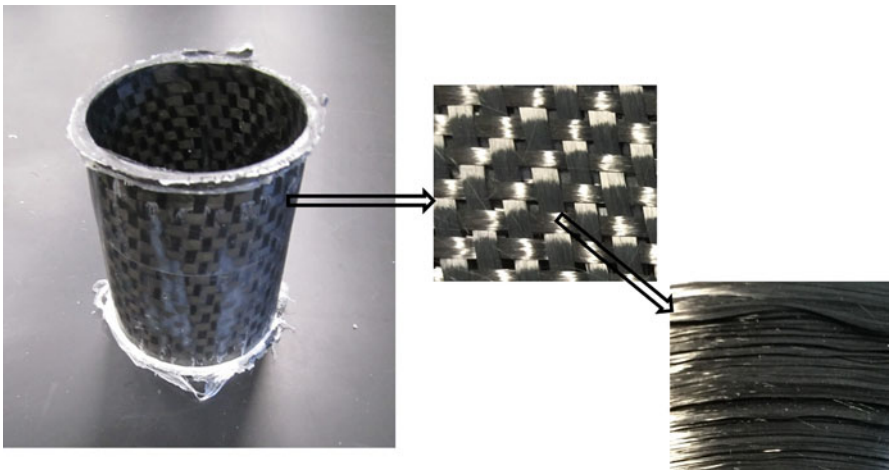

Fig. 28.2 Rough carbon fiber composite cylinder after removal from mold

28.3 Multiscale Analysis Technique

As described previously, in order to apply failure criteria at the constituent material level, a multiscale modeling technique was developed [21–29] for various types of composite materials such as particulate, fibrous, short fiber, and woven fabric composites. The multiscale analysis technique is based on the constituent materials. The final composite structure is constructed analytically from the constituent materials. For example, Fig. 28.2 shows the hierarchy of a woven fabric composite cylinder. The composite cylinder was fabricated by wrapping the plain weave fabrics which consists of the weft and warp. The fabric was made of fibers. Then, resin or epoxy matrix materials were applied to the fiber materials. This is illustrated by the arrows in Fig. 28.2.

As a result, the multiscale analysis technique computes the material properties of the composite cylinders using the hierarchy of the structure and the constituent material properties. Figure 28.3 sketches the multiscale analysis technique. Especially, the forward loop in the figure is the process to compute the effective material properties of the composite cylinder. The material properties of the fibrous composite are computed from the material properties of the fiber and matrix. Then, the material properties of the woven fabric are calculated from the fibrous composite properties and the weave architecture. If local damage or failure occurs and progresses, these computations must be conducted repeatedly. Hence, detailed numerical models of the unidirectional and woven fabric composites are not practical. The computational cost would be very expensive. In order to make the analysis process computationally efficient, analytical models were developed based on the concept of a repeated unit-cell model. Hence, the forward loop or called stiffness loop does not require any major numerical computations.

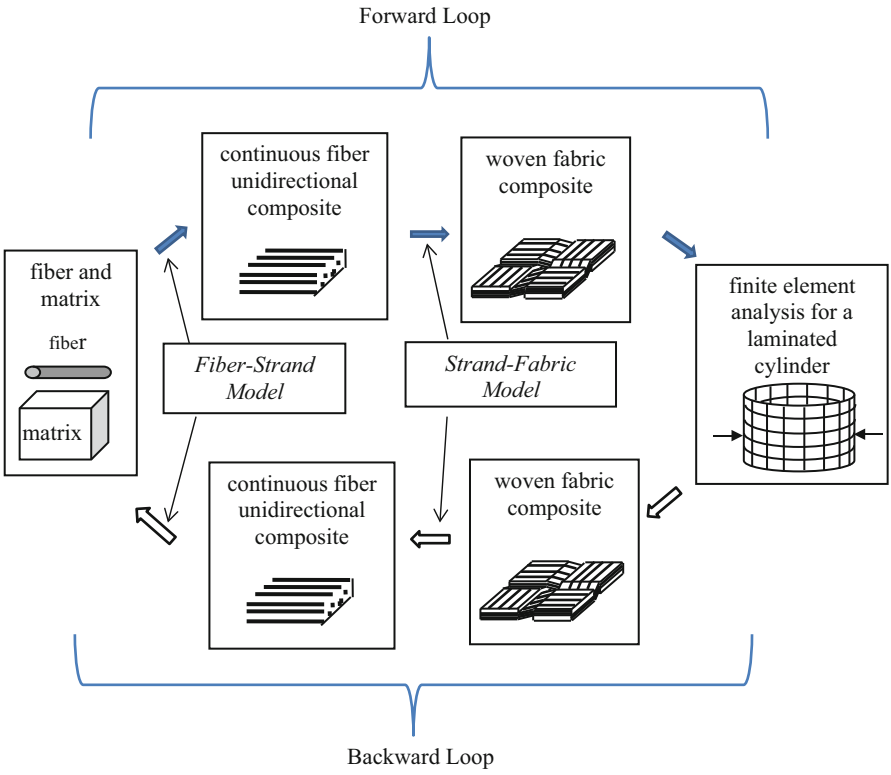

Fig. 28.3 Multiscale analysis process

Once the effective material properties of the carbon composite cylinder are determined, a finite element analysis is conducted for the composite cylinder which is subjected to given loading and boundary conditions. Even though the eventual analysis is for explosive loading inside the carbon fiber composite cylinder, the current study was focused on static internal pressure loading as described later. There are a couple of different ways to model laminated composite structures. One is to model the whole layers as a single element. When this is undertaken, there are two choices. The whole layers are smeared into an equivalent single layer using the lamination theory [11, 30–32]. The other alternative is to use multiple numerical integration points through the thickness of the whole layer such that different material properties at different layers can be considered at those numerical integration points. The latter is more effective than the former. One drawback of the both techniques is their difficulty with modeling any delamination between two neighboring layers, which is a very common damage mode. In order to overcome this, each layer can be modeled using a separate finite element. However, modeling each layer using 3-D solid elements is not numerically plausible because the element aspect ratio would be so huge. Instead, shell elements are used. In order to have shell

elements layered on top of another, 3-D solid-like shell elements would be useful [33–38]. In other words, the 3-D-like shell element uses the shell formulation but has displacements as nodal degrees of freedom without rotational degrees of freedom. Because the nodes are located at the bottom and top surfaces of the shell element, those shell elements can be stacked one another like 3-D solid elements. However, the shell element can represent a large aspect ratio of the element. If necessary, resin layers between two composite layers can be modeled explicitly to represent potential delamination. Previous studies [39, 40] showed that modeling those resin layers explicitly was important to predict delamination damage accurately.

The finite element analysis provides deformations, strains, and stresses of the composite structure. Those strains and stresses are the effective strains and stresses at each lamina level. If a laminar level failure criterion, as expressed in Eqs. (28.2) and (28.5), is used, these stresses components are used directly. However, in the present multiscale analysis technique, those strains and stresses are decomposed to the strains and stresses at the constituent material level such as fiber and matrix. In order to accomplish this, the same analytical unit-cell models used in the forward loop are used and this process is called "backward loop" as shown in Fig. 28.3. The backward loop is also called the strength loop.

The two analytical models are called fiber-strand and strand-fabric whose unit-cells are sketched in Fig. 28.4. As stated, the both models utilize unit-cell models. They compute the effective material properties in the forward loop. In other words, the fiber-strand model determines the effective material properties of the unidirectional composites made of fiber and matrix materials, while the strand-fabric model computes the effective material properties of the woven fabric composite using the geometric data of the woven fabric and the unidirectional composite materials. The effective properties of the woven fabric are used for the finite element analysis of a composite cylinder subjected to a given applied load.

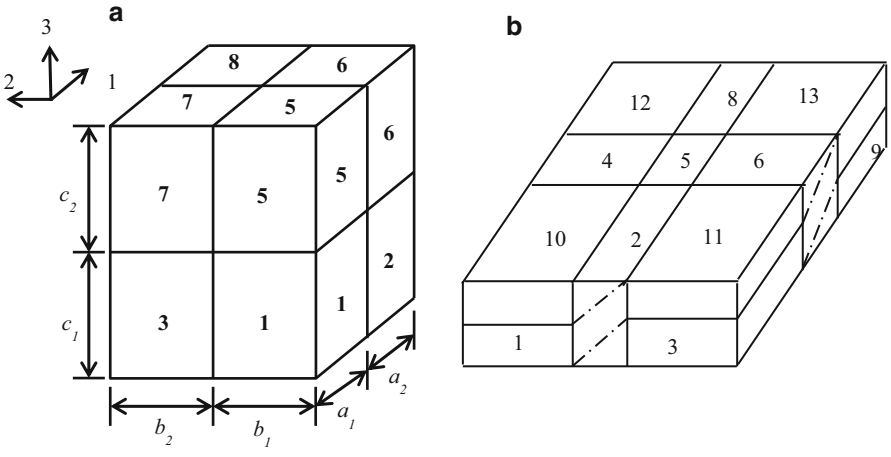

Fig. 28.4 Unit-cell models for (**a**) fiber-strand and (**b**) strand-fabric models

If an analytical solution is available, it can be used instead. Either the finite element analysis or analytical solution gives macro-level stresses and strains in the composite cylinder. These macro-level stresses and strains are decomposed to the microlevel stresses and strains at the fiber and matrix level using the same two models through the backward loop.

The failure of the cylinder is determined when the fiber reaches the tensile strength of the material. The failure criteria at the constituent material level are expressed as below. The carbon fiber failure is tested using the following equation:

$$\sigma_f = f_t \quad \text{if} \quad \sigma_f > 0 \tag{28.6a}$$

$$\left|\sigma_f\right| = f_c \quad \text{if} \quad \sigma_f < 0 \tag{28.6b}$$

where σ_f is the stress which the fiber carries along the fiber direction and f_t and f_c are the fiber strength in tension and compression, respectively. The compressional strength also considers fiber micro-buckling [41, 42]. For the resin material, the principal strain criterion is used as shown below:

$$(\varepsilon_m)_{\max} = e_t \quad \text{if} \quad (\varepsilon_m)_{\max} > 0 \tag{28.6c}$$

$$|(\varepsilon_m)_{\min}| = e_c \quad \text{if} \quad (\varepsilon_m)_{\min} < 0 \tag{28.6d}$$

in which $(\varepsilon_m)_{\max}$ and $(\varepsilon_m)_{\min}$ are the maximum and minimum principal strains of the matrix material and e_t and e_c are the failure strain in tension and compression, respectively.

To save space, only some details of the fiber-strand model are presented below, while the strand-fabric model is omitted because the basic assumptions and formulations are similar between the two modules. Details of the modules are presented in Ref. [21–25].

The unit-cell model for the fiber-strand model is comprised of a rectangular prism divided into eight quadrants or subcells as shown in Fig. 28.4. Each subcell can be identified as a different material, and the unit-cell model can solve for equivalent composite elastic moduli, Poisson's ratio, and the coefficient of thermal expansion. The following equations define the equilibrium stress state at the interfaces of the subcells:

$$\sigma_{11}^1 = \sigma_{11}^2 \quad \sigma_{11}^3 = \sigma_{11}^4 \quad \sigma_{11}^5 = \sigma_{11}^6 \quad \sigma_{11}^7 = \sigma_{11}^8 \tag{28.7a}$$

$$\sigma_{22}^1 = \sigma_{22}^3 \quad \sigma_{22}^2 = \sigma_{22}^4 \quad \sigma_{22}^5 = \sigma_{22}^7 \quad \sigma_{22}^6 = \sigma_{22}^8 \tag{28.7b}$$

$$\sigma_{33}^1 = \sigma_{33}^5 \quad \sigma_{33}^2 = \sigma_{33}^6 \quad \sigma_{33}^3 = \sigma_{33}^7 \quad \sigma_{33}^4 = \sigma_{33}^8 \tag{28.7c}$$

$$\sigma_{12}^1 = \sigma_{12}^2 = \sigma_{12}^3 = \sigma_{12}^4 \quad \sigma_{12}^5 = \sigma_{12}^6 = \sigma_{12}^7 = \sigma_{12}^8 \tag{28.8a}$$

$$\sigma_{13}^1 = \sigma_{13}^2 = \sigma_{13}^5 = \sigma_{13}^6 \quad \sigma_{13}^3 = \sigma_{13}^4 = \sigma_{13}^7 = \sigma_{13}^8 \tag{28.8b}$$

$$\sigma_{23}^1 = \sigma_{23}^3 = \sigma_{23}^5 = \sigma_{23}^7 \quad \sigma_{23}^2 = \sigma_{23}^4 = \sigma_{23}^6 = \sigma_{23}^8 \tag{28.8c}$$

Here, the first three sets of equations are for the normal stresses, and the other three sets are for the shear stresses.

The subscripts denote stress components according to the axis in Fig. 28.4, while the superscripts indicate subcell number. In addition to stress equilibrium, deformation compatibility must be met for the unit cell. Deformation compatibility defines the following set of equations:

$$a_1\varepsilon_{11}^1 + a_2\varepsilon_{11}^2 = a_1\varepsilon_{11}^3 + a_2\varepsilon_{11}^4 = a_1\varepsilon_{11}^5 + a_2\varepsilon_{11}^6 = a_1\varepsilon_{11}^7 + a_2\varepsilon_{11}^8 \tag{28.9a}$$

$$b_1\varepsilon_{22}^1 + b_2\varepsilon_{22}^3 = b_1\varepsilon_{22}^2 + b_2\varepsilon_{22}^4 = b_1\varepsilon_{22}^5 + b_2\varepsilon_{22}^7 = b_1\varepsilon_{22}^6 + b_2\varepsilon_{22}^8 \tag{28.9b}$$

$$c_1\varepsilon_{33}^1 + c_2\varepsilon_{33}^5 = c_1\varepsilon_{33}^2 + c_2\varepsilon_{33}^6 = c_1\varepsilon_{33}^3 + c_2\varepsilon_{33}^7 = c_1\varepsilon_{33}^4 + c_2\varepsilon_{33}^8 \tag{28.9c}$$

$$\begin{aligned}&(a_1b_1)\,\varepsilon_{12}^1 + (a_2b_1)\,\varepsilon_{12}^2 + (a_1b_2)\,\varepsilon_{12}^3 + (a_2b_2)\,\varepsilon_{12}^4 \\ &\quad = (a_1b_1)\,\varepsilon_{12}^5 + (a_2b_1)\,\varepsilon_{12}^6 + (a_1b_2)\,\varepsilon_{12}^7 + (a_2b_2)\,\varepsilon_{12}^8\end{aligned} \tag{28.10a}$$

$$\begin{aligned}&(a_1c_1)\,\varepsilon_{13}^1 + (a_2c_1)\,\varepsilon_{13}^2 + (a_1c_2)\,\varepsilon_{13}^5 + (a_2c_2)\,\varepsilon_{13}^6 \\ &\quad = (a_1c_1)\,\varepsilon_{13}^3 + (a_2c_1)\,\varepsilon_{13}^4 + (a_1c_2)\,\varepsilon_{13}^7 + (a_2c_2)\,\varepsilon_{13}^8\end{aligned} \tag{28.10b}$$

$$\begin{aligned}&(b_1c_1)\,\varepsilon_{23}^1 + (b_2c_1)\,\varepsilon_{23}^3 + (b_1c_2)\,\varepsilon_{23}^5 + (b_2c_2)\,\varepsilon_{23}^7 \\ &\quad = (b_1c_1)\,\varepsilon_{23}^2 + (b_2c_1)\,\varepsilon_{23}^4 + (b_1c_2)\,\varepsilon_{23}^6 + (b_2c_2)\,\varepsilon_{23}^8\end{aligned} \tag{28.10c}$$

Furthermore, each subcell has a constitutive equation defining strain as below:

$$\varepsilon_{ij}^n = C_{ijkl}^n\sigma_{kl}^n + \alpha_{ij}^n\Delta\theta \tag{28.11}$$

For this model, the thermal expansion of the materials is ignored.

The total unit-cell stress and strain can then be found by averaging the subcell stresses and strains based on subcell volume:

$$\overline{\sigma}_{ij} = \sum_{n=1}^{8} V^n\sigma_{ij}^n \tag{28.12}$$

$$\overline{\varepsilon}_{ij} = \sum_{n=1}^{8} V^n\varepsilon_{ij}^n \tag{28.13}$$

Because most of fiber and matrix materials are either isotropic or orthotropic, the normal and shear components are decoupled. As a result, the two components can be worked out independently. The mathematical development of the two components is very similar. Therefore, only the normal components are discussed here. Arranging above equations for the normal components yields the following equation:

$$[T]\{\varepsilon\} = \{f\} \tag{28.14}$$

where $[T]$ is a 24×24 matrix with the combination of three vectors containing stress relationships, strain relationships, and constitutive equations:

$$[T]^T = [[T1] \quad [T2] \quad [T3]] \tag{28.15}$$

Here, $[T1]$ is a 24×12 matrix of normal stress relationships, $[T2]$ is a 24×9 matrix of normal strain relationships, and $[T3]$ is a 24×3 matrix of constitutive equations. Then, $\{f\}$ is a 24×1 column vector composed of a 21×1 column containing zeros and a 3×1 column containing the effective normal strains.

$$\{f\}^T = \left\{ \{0\} \left\{ \overline{\varepsilon}_{11} \ \overline{\varepsilon}_{22} \ \overline{\varepsilon}_{33} \right\} \right\} \tag{28.16}$$

Solving Eq. (28.14) produces the following equation:

$$\{\varepsilon\} = [T]^{-1}\{f\} \tag{28.17}$$

The inverse of $[T]$ can be further broken down into three submatrices. These can be expressed like the following:

$$[T]^{-1} = [[R1] \quad [R2] \quad [R3]] \tag{28.18}$$

$$\{\varepsilon\} = [R3]\left\{ \overline{\varepsilon}_{11} \ \overline{\varepsilon}_{22} \ \overline{\varepsilon}_{33} \right\}^T \tag{28.19}$$

Furthermore, Eq. (28.12) can be written as:

$$\{\overline{\sigma}\} = [V]\{\sigma\} \tag{28.20}$$

As Eqs. (28.11) and (28.19) are substituted into Eq. (28.20), the following unit-cell stress expression is found:

$$\{\overline{\sigma}\} = [V]([E]\{\varepsilon\}) = [V][E][R3]\{\overline{\varepsilon}\} \tag{28.21}$$

where $[E]$ is a matrix of the inverse of the subcell compliance tensors stated in Eq. (28.11). Then, the unit-cell stiffness can be calculated:

$$\left[\overline{E}\right] = [V][E][R3] \tag{28.22}$$

The $[\bar{E}]$ matrix found through Eq. (28.22) is the 3×3 matrix of the unit-cell stiffness. With these values, Poisson's ratio of the unit cell can also be found. A similar method can be utilized to solve for the shear properties of the composite material.

For the strength loop, Eq. (28.17) is used to compute constituent material level strains from the composite level strains. Then, Eq. (28.11) is also used to compute the stresses in the fiber and matrix materials. Hence, this module can complete both forward and backward loops.

28.4 Experimental Device

Before conducting explosive testing for carbon composite cylinders, static internal pressure loading was considered for the composite cylinders. As a result, a mechanical device was developed to apply internal pressure loading to a composite cylinder instead of using pressurized fluids. The device is sketched in Fig. 28.5, and it consists of multiple parts. The two upper and bottom rams are used to apply the axial loading using a uniaxial mechanical testing machine. The eight equal sizes of wedges are utilized to transfer the axial loading to the radial loading like internal pressure loading. The guide pin is used to maintain the rams in the collinear axis. A shim may be used between the composite cylinder and the wedges if there is a small gap in the beginning before applying the load.

Figures 28.6 and 28.7 show the free body diagrams for the ram and wedge. After applying the equilibrium equations and assuming Coulomb's friction law, the internal pressure p_i is related to the axial load F as below:

$$p_i = \frac{F}{\pi a L}\left(\frac{\tan\,\theta - \mu}{1 + \mu\,\tan\,\theta}\right) \tag{28.23}$$

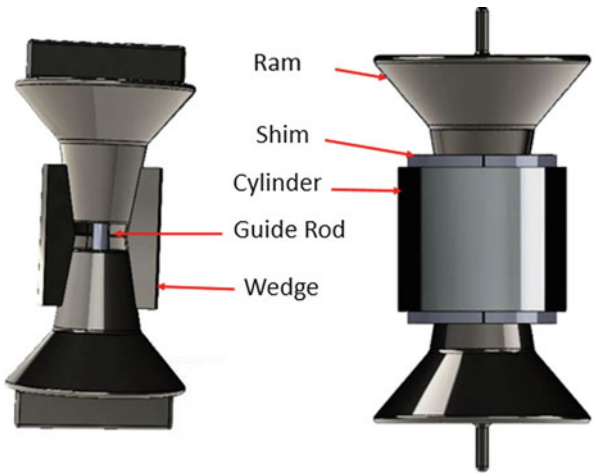

Fig. 28.5 Mechanics device for internal pressure loading

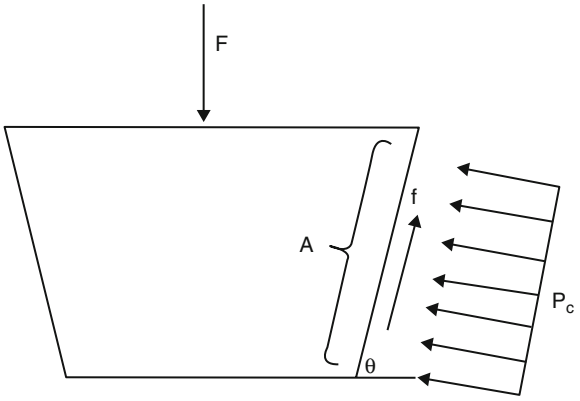

Fig. 28.6 Free body diagram for ram

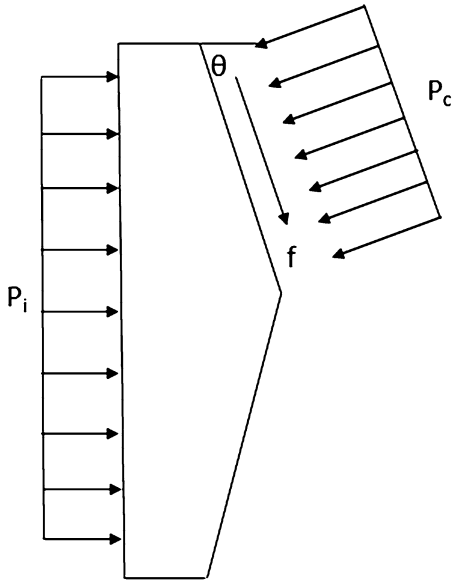

Fig. 28.7 Free body diagram for wedge

where μ is the coefficient of friction, θ is the angle shown in Figs. 28.6 and 28.7, and a and L are the outer radius and the length of the wedge. The present wedge has the angle $\theta = 80°$

For an axisymmetric cylinder, the hoop strains at the inner and outer surfaces of the cylinder are written as

$$\varepsilon_h^i = \frac{a^2 p_i}{E\left(b^2 - a^2\right)}\left[(1-\nu) + (1+\nu)\frac{b^2}{a^2}\right] \tag{28.24}$$

$$\varepsilon_h^o = \frac{2a^2 p_i}{E\left(b^2 - a^2\right)} \tag{28.25}$$

in which a, b, and E are the inner and outer radii and the elastic modulus of the cylinder. From Eqs. (28.23) to (28.25), we obtain the following expression:

$$\varepsilon_h^o = \frac{2aF}{\pi E\left(b^2 - a^2\right)L}\left(\frac{\tan\theta - \mu}{1 + \mu\tan\theta}\right) \tag{28.26}$$

and

$$\varepsilon_h^i = \frac{aF}{\pi E\left(b^2 - a^2\right)L}\left[(1 - \nu) + (1 + \nu)\frac{b^2}{a^2}\right]\left(\frac{\tan\theta - \mu}{1 + \mu\tan\theta}\right) \tag{28.27}$$

The hoop stress at the inner wall of the cylinder is

$$\sigma_h^i = \frac{\left(a^2 + b^2\right)F}{\pi E\left(b^2 - a^2\right)aL}\left[\frac{\tan\theta - \mu}{1 + \mu\tan\theta}\right] \tag{28.28}$$

As the thickness of the cylinder becomes much smaller than the cylinder radius, Eq. (28.28) is simplified as

$$\sigma_h^i = \frac{F}{\pi EtL}\left[\frac{\tan\theta - \mu}{1 + \mu\tan\theta}\right] \tag{28.29}$$

The material used for the device should be very stiff and strong such that the device has a minimal deformation and does not yield during the test. Of course, this requirement is relative to the cylinder material. To this end, the 1704 PH stainless steel was selected for the device material. In order to validate the application of the device for internal pressure loading, a finite element analysis (FEA) was conducted for the device with a 6061 T6 aluminum alloy cylinder which has the height 7.62 cm (3 in), the inside diameter 7.62 cm (3 in), and the wall thickness 0.3175 cm (0.125 in). In the finite element model, the bottom ram was fixed, while the top ram was pushed down for a specific distance. The distance was determined using the expected hoop strain in the cylinder assuming the rams and wedges were rigid. This expected strain was called the target hoop strain which was ranging from 0.001 to 0.01. Because the rams and wedges are not rigid materials, there should be some difference between the target strain and the FEA strain. For this study, the coefficient of fiction was assumed 0.01. The stainless steel has the elastic modulus 200 GPa and Poisson's ratio 0.28, while the aluminum alloy has the elastic modulus 68.9 GPa and Poisson's ratio 0.33. Since elastic analysis was conducted for FEA, the stress level was lower than yield strength of both materials. Table 28.1 compares the target strain and the FEA strain at different strain levels. The difference is about 7 %. Because of the deformation in the rams and wedges, the FEA strains were smaller than the target strain. If there is no measurement of strain, the target strain may be used as a conservative representation of the actual strain. However, in the following studies, a hoop strain was measured using a strain gauge (Tables 28.2 and 28.3).

Table 28.1 FEA result for aluminum cylinder

Target hoop strain	0.001	0.002	0.003	0.004
FEA hoop strain	0.000931	0.001855	0.002779	0.003706
Error	−6.92 %	−7.28 %	−7.37 %	−7.36 %

Table 28.2 Properties of carbon fiber and matrix materials

	E_L (GPa)	E_T (GPa)	G_{LT} (GPa)	G_{TT} (GPa)	γ_{LT}	γ_{TT}	Tensile strength (MPa)	Shear strength (MPa)
Carbon fiber	221	13.8	13.8	5.5	0.20	0.25	3538	–
Matrix	4.4	4.4	1.6	1.6	0.34	0.34	159	100

Table 28.3 Comparison of properties of unidirectional fibrous composite (fiber volume fraction 0.7)

	E_L (GPa)	E_T (GPa)	γ_{LT}	γ_{TT}	Long strength (MPa)	Transverse strength (MPa)
Present	156	10.2	0.24	0.54	2543	148
Ref. [43]	151	10.1	0.24	0.50	2550	152

28.5 Results and Discussion

The multiscale analysis technique has been validated against many experimental data, especially for the effective material properties at different length scales. For example, effective material properties of the fibrous and woven fabric composites were studied. Table 28.2 shows the material properties of the fiber and matrix materials [43]. Then, the effective material properties of the unidirectional composite made of the fiber and matrix materials were computed using the fiber-strand unit-cell model and compared to the data in Ref. [43]. Both effective stiffness and strength results agreed very well each other [23]. The next example examined a plain weave composite made of carbon/epoxy materials as given in Table 28.4 [44] using the strand-fabric unit-cell model. The computed effective stiffness of the plain weave fabric was compared to the experimental data [23, 44, 45]. The predicted solution agreed well with the published data.

Then, the whole multiscale analysis technique was applied to the present carbon composite cylinders. Before applying the multiscale analysis technique to carbon composite cylinders, uniaxial tensile coupons were considered. The test coupons were fabricated using the same plain weave composites made of carbon fibers. The purpose of these coupons and tensile tests was to check the material properties of the composite. Both tensile coupons and cylinders had woven layers 0°/90° so that the laminated composites were quasi-isotropic. Figure 28.8 shows the carbon composite tensile test coupons after failure. A set of strain gauges were attached to each test coupon, one in the axial direction and the other in the transverse direction. Figure 28.9 shows a typical stress-strain plot of the carbon composite coupon.

Table 28.4 Material properties of carbon/epoxy strands and resin

	E_L (GPa)	E_T (GPa)	G_{LT} (GPa)	G_{TT} (GPa)	γ_{LT}	γ_{TT}
Carbon/epoxy	134	10.2	5.52	3.43	0.30	0.49
Epoxy	3.45	3.45	1.28	1.28	0.35	0.35

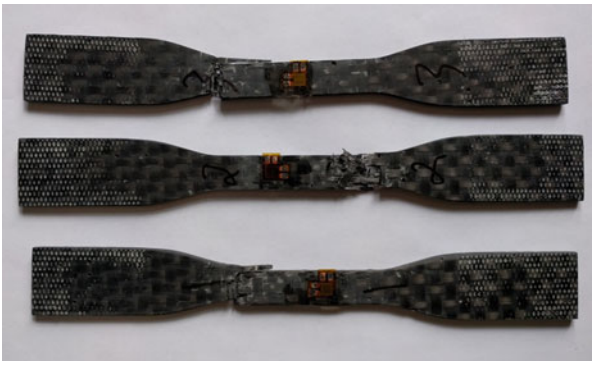

Fig. 28.8 Tensile specimens after testing

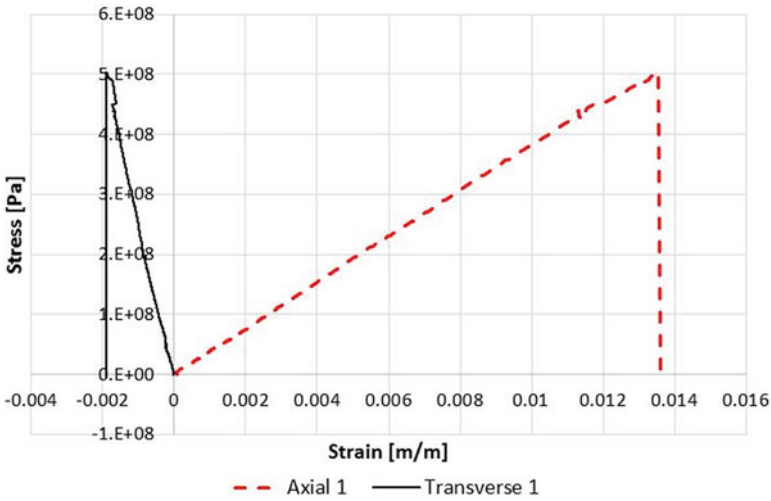

Fig. 28.9 Tensile test data

The elastic modulus was determined from the stress-strain curve and it is 40.0 GPa and the Poisson's ratio is 0.14. The stress at failure is 500 MPa, and the specimen fractured at the maximum strain of 0.0135 m/m (Table 28.5).

The multiscale analysis model depicted in Fig. 28.3 was used to predict the material behavior of the tensile test coupon. Both fiber-strand and strand-fabric models were used one after the other sequentially. The multiscale analysis requires fiber and matrix material properties as well as their volume fractions and geometric data of the plain weave architecture. The elastic modulus of the carbon fiber is 230 GPa and Poisson's ratio is 0.2. The carbon fiber has the tensile strength

Table 28.5 Comparison of stiffness of plain weave composite made of carbon fiber and epoxy

	E_L (GPa)	E_T (GPa)	G_{LT} (GPa)	G_{TT} (GPa)	γ_{LT}	γ_{TT}
Present	54.9	10.2	4.28	3.47	0.02	0.47
Ref. [44]	55.5	–	4.93	–	0.06	–
Ref. [45]	56.1	10.4	5.08	3.71	0.03	0.59

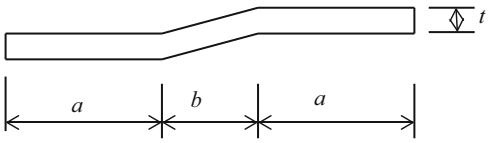

Fig. 28.10 Sketch of single strand in plain weave composite

3530 MPa and the fracture strain 0.015 m/m. On the other hand, the elastic modulus of the matrix material is 1.64 GPa, and Poisson's ratio is 0.33. The fiber volume fraction for the unidirectional model used for the fiber-strand model was assumed to be 0.35. The plain weave fabric has the geometric data $a = 4$ mm, $b = 1.5$ mm, and $t = 0.25$ mm as sketched for a single tow strand in Fig. 28.10. Some of these data were measured, while others were obtained from the manufacture specifications.

The multiscale analysis computed the effective elastic modulus and the fracture strain of the carbon composite tensile coupon. First of all, the fiber-strand model resulted in the effective modulus of the unidirectional fibrous composite equal to 81.6 GPa, and the effective modulus of the woven fabric was 39.9 GPa. The Poisson's ratio of the fabric was 0.014. Both of these values agreed well with the tensile test data. The fracture strain was 0.013 m/m. The fracture strain was computed when the carbon fibers reached their failure strength as provided above. The predicted values were in good agreement with the measured data. This gave a good confirmation that the constituent material properties as well as other geometric data were reasonable. Then, the same data were used for the subsequent study for composite cylinder subjected to internal pressure loading.

Carbon composite cylinders were tested using the mechanical device described previously. In order to correlate the applied axial force F to internal pressure, the coefficient of friction is needed. To determine the coefficient, an aluminum alloy cylinder was used, while strain gauges were attached to the aluminum alloy cylinder. The applied force and the hoop strain at the outside surface of the cylinder were substituted to Eq. (28.26) to determine the coefficient of friction between the rams and wedges. The coefficient of friction was 0.12 from the test. Figure 28.11 compares the experimental data from the aluminum cylinder and the result from Eq. (28.26) with the coefficient of friction 0.12. They agreed very well as long as the cylinder deformed in the linear elastic range. Once there was plastic deformation, Eq. (28.26) is not valid any more. However, this is not a concern for the carbon fiber composite cylinder because the carbon composite behaves linearly until fracture. Furthermore, it is a reasonable assumption that the coefficient of friction remains constant independent of the loading magnitude as long as the same lubricant is used.

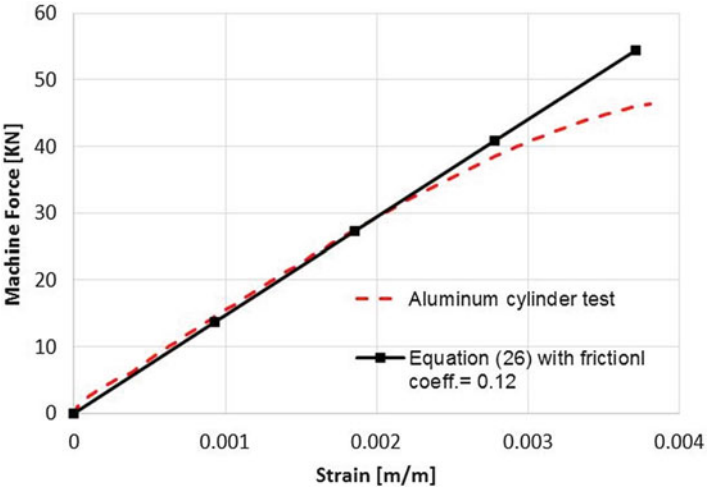

Fig. 28.11 Frictional coefficient obtained from aluminum cylinder test

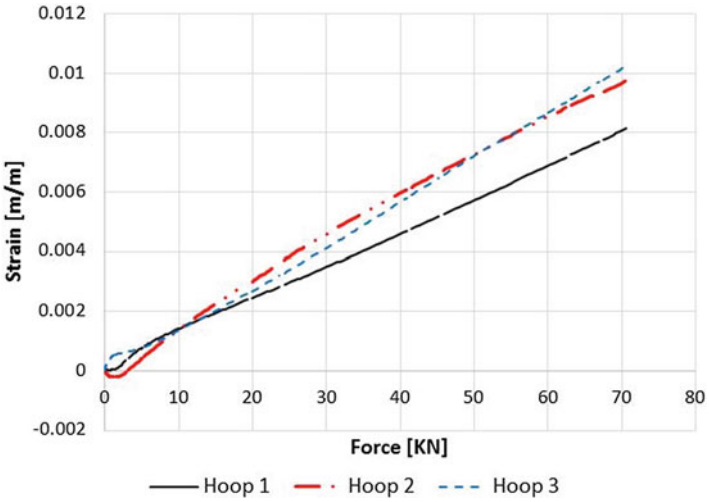

Fig. 28.12 Test result of composite cylinder

Experiments were undertaken for three composite cylinders whose inner radius is 7.62 cm (3 in). There is some variation in thickness with the average wall thickness 2.5 mm. A typical load vs. strain curves are plotted for a carbon composite cylinder in Fig. 28.12. Three strain gauges were attached to the cylinder along the circumferential direction. The whole set of wedges consists of eight pieces. As a result, the wedges are piecewise continuous along the circumference of the cylinder. As the wedges push out the cylinder, the cylinder locations corresponding to gaps between two neighboring wedges experience less strains compared to other

locations. Figure 28.12 confirms this observation. In the figure, the hoop strain gauge #1 was placed at the cylinder location between two wedges, while the other two hoop strain gauges were placed at the cylinder locations corresponding to the middle of the wedges. Therefore, strain gauge #1 yielded a lower strain than the others which were very close.

Because strain gauges #2 and 3 represent the response of the cylinder under internal pressure loading better than gauge #1, the failure load and strain were obtained from the two strain gauges. The failure load was 70 kN and the fracture hoop strain was 0.010. Those values were compared to the results from the multiscale analysis. The initial results showed that the predicted failure strain was about 25 % lower than the experimental value. The initial model assumed a uniform wall thickness. However, the actual measurement of the cylinders showed that the wall thickness varied 6 % around the cylinder. Because the cylinder was fabricated as shown in Fig. 28.1, resins flew down during the curing process. As a result, the bottom side of the cylinder was thicker than the top side in Fig. 28.1. Considering this, a new FEA was conducted with a gradual change in thickness along the hoop direction, and the multiscale analysis was also conducted along with the new FEA model. The predicted failure hoop strain was 0.0098 m/m, and the predicted maximum force was 76 kN which was equivalent to the internal pressure 13 MPa. These numerical values were in good agreement with the experimental results of the composite cylinders.

28.6 Conclusions

A new mechanical device consisting of rams and wedges were designed and manufactured so that internal pressure loading can be applied to the inside of a cylinder without using any fluid. Then, carbon composite cylinders were tested using the new mechanical device to determine their failure load/pressure and the fracture strain. The experimentally measured values were compared to the values predicted using the multiscale analysis model. The two results agreed very well. One parameter is required in the mechanical device, which is the coefficient of friction between the rams and wedges. The coefficient was obtained from an experimental study on an aluminum alloy cylinder by measuring the applied axial force and the hoop strain on the cylinder. For the current device, the coefficient was 0.12.

The success of the developed mechanical device for internal pressure loading as well as the reliable multiscale analysis technique will lead to initial designs of carbon composite cylinders containing high explosive materials. Then, limited tests will be conducted for the composite cylinders with the high explosive loading to refine the design. Eventually, carbon fiber composites will be designed and used for extreme loading environment because of high strength and stiffness with low density.

References

1. A.M. Clayton, A simplified method to determine initial estimates of peak strains in composite explosive containment vessels. ASME Paper No. PVP2013-97068, 2013 ASME Pressure Vessels and Piping Conference, Paris, France, 14–18 July 2013
2. A.G. Fedorenko, M.A. Syrunin, A.G. Ivanov, Criterion for selecting composite materials for explosion containment structures (review). Combust. Explos. Shock Waves **41**(5), 487–495 (2005)
3. J.W. Pastrnak, C.D. Henning, W. Grundler, Composite vessels for containment of extreme blast loading. Lawrence Livermore National Laboratory, Technical Report No. UCRL-CONF-205423 (2004)
4. Q. Dong, Q.M. Li, J.Y. Zheng, B.Y. Hu, Effects of structural perturbations on strain growth in containment vessels. ASME J. Press. Vessel Technol. **132**, 011203 (2010)
5. Q. Dong, B. Hu, Dynamic behavior of carbon fiber explosion containment vessels. ASME J. Press. Vessel Technol. **138**, 011292 (2016)
6. Z. Hashin, Failure criteria for unidirectional fiber composites. J. Appl. Mech. **47**, 329–334 (1980)
7. G.P. Sendeckyi, A brief survey of empirical multiaxial strength criteria for composites. *Composite Materials: Testing and Design*, ASTM STP 497 (1972), pp. 41–51
8. E.M. Wu, Phenomenological anisotropic failure criterion, ed. by G.P. Sendeckyj, in *Composite Materials Volume 2, Mechanics of Composite Materials* (Academic Press, New York, 1974), pp. 253–431
9. C.C. Chamis, Failure criteria for filamentatry composites. *Composite Materials: Testing and Design*, ASTM STP 460 (1969), pp. 336–351
10. B.E. Kaminski, R.B. Lantz, Strength theories of failure for anisotropic materials. *Composite Materials: Testing and Design*, ASTM STP 460 (1969), pp. 160–169
11. S.W. Tsai, H.T. Hahn, *Introduction to Composite Materials* (Technomic Publishing Co., Lancaster, 1980)
12. M.E. Waddoups, Advanced composite material mechanics for the design and stress analyst. General Dynamics, Fort Worth Division Report FZM-4763 (1967)
13. M. Xia, K. Kemmochi, H. Takayanagi, Analysis of filament-wound fiber-reinforced sandwich pipe under combined internal pressure and thermomechanical loading. Compos. Struct. **5**, 273–283 (2001)
14. P.D. Soden, R. Kitching, P.C. Tse, Experimental failure stresses for $\pm 55^\circ$ filament wound glass fiber reinforced plastic tubes under biaxial loads. Composites **20**, 125–135 (1989)
15. J. Mistry, A.G. Gibson, Y.-S. Wu, Failure of composite cylinders under combined external pressure and axial loading. Compos. Struct. **22**, 193–200 (1992)
16. M. Uemura, H. Fukunaga, Probabilistic burst strength of filament-wound cylinders under internal pressure. J. Compos. Mater. **15**, 462–480 (1981)
17. A. Onder, O. Sayman, T. Dogan, N. Tarakcioglu, Burst failure load of composite pressure vessels. Compos. Struct. **89**, 159–166 (2009)
18. M. Xia, H. Takayanagi, K. Kemmochi, Analysis of multi-layered filament-wound composite pipes under internal pressure. Compos. Struct. **53**, 483–491 (2001)
19. J. Xing, P. Geng, T. Yang, Stress and deformation of multiple winding angle hybrid filament-wound thick cylinder under axial loading and internal and external pressure. Compos. Struct. **131**(4), 866–877 (2015)
20. T. Hwang, J. Park, H. Kim, Evaluation of fiber material properties in filament-wound composite pressure vessels. Compos. Part A **43**, 1467–1475 (2012)
21. Y.W. Kwon, *Multiphysics and Multiscale Modeling: Techniques and Applications* (CRC Press, Boca Raton, 2016)
22. Y.W. Kwon, Multi-level approach for failure in woven fabric composites. Adv. Eng. Mater. **3**(9), 713–717 (2001) (Invited Paper)

23. Y.W. Kwon, A. Altekin, Multi-level, micro-macro approach for analysis of woven fabric composites. J. Compos. Mater. **36**(8), 1005–1022 (2002)
24. Y.W. Kwon, M.S. Park, Versatile micromechanics model for multiscale analysis of composite structures. Appl. Compos. Mater. **20**(4), 673–692 (2013)
25. M.S. Park, Y.W. Kwon, Elastoplastic micromechanics model for multiscale analysis of metal matrix composite structures. Comput. Struct. **123**, 28–38 (2013)
26. Y.W. Kwon, J.M. Berner, Micromechanics model for damage and failure analyses of laminated fibrous composites. Eng. Fract. Mech. **52**(2), 231–242 (1995)
27. Y.W. Kwon, C.T. Liu, Study of damage evolution in composites using damage mechanics and micromechanics. Compos. Struct. **38**(1–4), 133–139 (1997)
28. Y.W. Kwon, C. Kim, Micromechanical model for thermal analysis of particulate and fibrous composites. J. Therm. Stresses **21**, 21–39 (1998)
29. Y.W. Kwon, J.H. Lee, C.T. Liu, Modeling and simulation of crack initiation and growth in particulate composites. Trans. ASME J. Press. Vessel Technol. **119**(3), 319–324 (1997)
30. R.F. Gibson, *Principles of Composite Material Mechanics* (McGraw-Hill, New York, 1994)
31. B.D. Agarwal, L.J. Broutman, *Analysis and Performance of Fiber Composites* (Wiley, New York, 1980)
32. R.M. Jones, *Mechanics of Composite Materials*, 2nd edn. (Taylor & Francis, Philiadelphia, 1999)
33. D.R.J. Owen, Z.H. Li, A refined analysis of laminated plates by finite element displacement methods—I: fundamentals and static analysis. Comput. Struct. **26**, 907–914 (1987)
34. Y.W. Kwon, Finite element analysis of crack closure in plate bending. Comput. Struct. **32**, 1439–1445 (1989)
35. G.M. Kulikov, S.V. Plotnikova, Finite rotation geometrically exact four-node solid-shell element with seven displacement degrees of freedom. Comput. Model. Eng. Sci. **28**, 15–38 (2008)
36. S. Klinkel, F. Gruttmann, W. Wagner, A continuum based three-dimensional shell element for laminated structures. Compos. Struct. **71**, 43–62 (1999)
37. R. Hauptmann, K. Schweizerhof, A systematic development of 'sold-shell' element formulations for linear and non-linear analyses employing only displacement degrees of freedom. Int. J. Numer. Meth. Eng. **42**, 49–69 (1998)
38. Y.W. Kwon, Analysis of laminated and sandwich composite structures using solid-like shell elements. Appl. Compos. Mater. **20**(4), 355–373 (2013)
39. M.F. Boseman, Y.W. Kwon, D. Loup, E. Rasmussen, Interface fracture of hybrid joint of glass-/steel-fiber composites. Eng. Comput. **29**(5), 504–527 (2012)
40. Y.W. Kwon, L.E. Craugh, Progressive failure modeling in notched cross-ply fibrous composites. Appl. Compos. Mater. **8**(1), 63–74 (2001)
41. B.W. Rosen (ed.), *Fiber Composite Materials* (American Society for Metals, Metals Park, 1965)
42. C. Soutis, P.T. Curtis, A method for predicting the fracture toughness of CFRP laminates failing by fibre microbuckling. Compos. Part A Appl. Sci. Manuf. **31**, 733–740 (2000)
43. D.M. Blackketter, D.E. Walrath, A.C. Hansen, Modeling damage in a plain weave fabric-reinforced composite material. J. Compos. Technol. Res. **15**(2), 136–142 (1993)
44. T. Ishikawa, M. Matsushima, Y. Hayashi, T.W. Chou, Experimental confirmation of the theory of elastic moduli of fabric composites. J. Compos. Mater. **19**(5), 443–458 (1985)
45. V.R. Aitharaju, R.C. Averill, Three-dimensional properties of woven-fabric composites. Compos. Sci. Technol. **59**, 1901–1911 (1999)